Journal of Materials Chemistry A

ROYAL SOCIETY OF CHEMISTRY

PAPER

View Article Online
View Journal | View Issue

Cite this: J. Mater. Chem. A, 2020, 8, 13285

Enveloping SiO_x in N-doped carbon for durable lithium storage *via* an eco-friendly solvent-free approach†

Guangwu Hu,‡[a] Kunzhe Zhong,‡[a] Ruohan Yu,[a] Zhenhui Liu,[a] Yuanyuan Zhang,[a] Jinsong Wu,[ab] Liang Zhou *[ac] and Liqiang Mai *[ac]

Silicon oxides, SiO_x, have aroused significant interests as high-capacity lithium-ion battery anode materials. To address the conductivity and volume fluctuation issues of SiO_x for practical applications, herein, we develop a novel eco-friendly, solvent-free, flammable gas-free approach to envelop SiO_x submicron particles in N-doped carbon (denoted as SiO_x@NC). The carbon encapsulation not only improves the electrical conductivity but also buffers the volume variation of SiO_x, resulting in boosted lithium storage performances. Specifically, the as-prepared SiO_x@NC affords high reversible capacity (774 mA h g^{-1}), ideal rate capability, and long-term durability (112% capacity retention over 500 cycles). It is expected that the solvent-free, flammable gas-free method we developed here can be generally applied to other high-capacity anode materials, such as Si, Sn, and Sb.

Received 14th January 2020
Accepted 20th June 2020

DOI: 10.1039/d0ta00540a

rsc.li/materials-a

Introduction

Lithium ion batteries (LIBs) play important roles in our daily life.[1–5] To meet the ever-increasing market requirements, it is imperative to develop LIBs with higher energy density without compromising power and safety.[6–10] As a key component, the anode material determines the electrochemical performances of LIBs to a certain degree. Graphite has been commercialized in LIBs owing to its high conductivity, stable layered structure, and moderate specific capacity.[11] Unfortunately, the Li^+ insertion/extraction potential of graphite is too close to the deposition of Li. This may result in the continuous and uneven deposition of Li on the surface, causing the formation of lithium dendrites and serious safety issues.[12,13]

Silicon oxides, SiO_x, have aroused significant attentions in recent years as a potential alternative LIB anode material.[14–23] When compared to elemental Si, the SiO_x has merits of smaller volume change, easier synthesis, and lower cost.[24–28] However, volume change still exists during the lithiation/delithiation of SiO_x, although it is not as large as that of elemental Si.[29–31] In addition, the electrical conductivity of SiO_x is unsatisfactory. These limitations lead to unsatisfactory cycling and rate performances, hampering the practical application of SiO_x.

To push the SiO_x towards practical applications, efforts have been dedicated to decorating the SiO_x with carbon.[6,32–40] For example, Oh *et al.* constructed carbon coated SiO through chemical vapor deposition (CVD).[41,42] Liu *et al.* design vertical graphene coated SiO with high capacity and ideal cyclability.[43] Guo *et al.* synthesized SiO_x/C based nanocomposites with enhanced structural integrity and cycling stability.[25,44,45] To date, the construction of SiO_x/C composites is generally based on either wet chemical method or CVD. As for the wet chemical method, the synthesis usually involves the employment of a large amount of solvents. The large consumption of solvents and the generation of waste water may cause an undesirable environmental issue. And the gases used in CVD process, such as methane and acetylene, are usually highly flammable and should be handled with great care. Therefore, the development of solvent-free, flammable gas-free approach towards SiO_x@carbon composites is of great significance.

Herein, we develop a solvent-free, flammable gas-free method for the scalable synthesis of SiO_x@N-doped carbon (SiO_x@NC). The SiO_x@NC shows improved electrical conductivity and structural integrity in lithium storage. As a result, the obtained SiO_x@NC manifests high reversible capacity with excellent durability. The eco-friendly synthesis as well as prominent electrochemical performances make the SiO_x@NC an ideal LIB anode material.

[a]State Key Laboratory of Advanced Technology for Materials Synthesis and Processing, Wuhan University of Technology, Wuhan 430070, P. R. China. E-mail: liangzhou@whut.edu.cn; mlq518@whut.edu.cn

[b]NRC (Nanostructure Research Centre), Wuhan University of Technology, Wuhan 430070, P. R. China

[c]Foshan Xianhu Laboratory of the Advanced Energy Science and Technology Guangdong Laboratory, Xianhu Hydrogen Valley, Foshan 528200, P. R. China

† Electronic supplementary information (ESI) available. See DOI: 10.1039/d0ta00540a

‡ Guangwu Hu and Kunzhe Zhong contributed equally to this work.

Experimental

Sample preparation

SiO_x submicron particles (denoted as SiO_x-BM) were prepared *via* high energy ball milling bulk SiO_x in Ar. The SiO_x-BM (0.126 g) were mixed with *m*-phenylenediamine (0.33 g), hexamethylenetetramine (HMTA, 0.1 g), and Pluronic F127 (0.83 g). The mixture was grinded in a glove box filled with Ar for 30 min. The mixture was then transferred into an autoclave and cured at 160 °C. After further annealing at 600 °C for 4 h in Ar, the SiO_x@NC were obtained. SiO_x@NC with a lower carbon content was also prepared by increasing the SiO_x-BM feeding amount to 0.252 g. Pure N-doped carbon (NC) was synthesized under the same conditions without adding SiO_x-BM. The SiO_x/NC was prepared by grinding a physical mixture of SiO_x-BM (0.126 g) and NC (0.236 g).

Characterization

Scanning electron microscopy (SEM) images were obtained with a JEOL-7100F microscope. Transmission electron microscopy (TEM) image was collected by a JEM-2100F microscope. High-angle annular dark field scanning transmission electron microscopy (HAADF-STEM) images and the energy dispersive X-ray spectrometry (EDS) measurements were performed on a Talos F200S microscope. Thermo gravimetric analysis (TGA) was performed on a STA-449C apparatus. X-ray diffraction (XRD) patterns were recorded using a Bruker D8 Advance X-ray diffractometer with a non-monochromated Cu Kα X-ray source (λ = 1.5418 Å). Raman spectra (200–2000 cm^{-1}) were recorded with a Renishaw INVIA Raman microscope. Particle size distribution (PSD) was collected on a NanoBrook 90Plus Zeta particle size distribution analyser. X-ray photoelectron spectroscopy (XPS) measurements were performed on a VG Multilab 2000 X-ray photoelectron spectrometer. Brunauer–Emmett–Teller (BET) surface areas were measured by a Tristar-3020 instrument.

Electrochemical measurements

For the preparation of working electrodes, active material, acetylene black, and sodium alginate (dissolved in deionized water) were mixed at a weight ratio of 7 : 2 : 1 in an agate mortar with grinding to form a homogeneous slurry. The slurry was coated onto a Cu foil, followed by drying at 70 °C for 12 h. The mass loading of active material was 1.0–1.5 mg cm^{-2}. Half-cells were assembled using the as-prepared working electrodes and lithium metal as the counter and reference electrodes in a glove box filled with Ar with 50 μl of electrolyte composed of 1.0 M lithium hexafluorophosphate ($LiPF_6$) in a mixture of ethylene carbonate/dimethyl carbonate (EC/DMC, 1 : 1 in volume) containing 5% fluoroethylene carbonate (FEC). Galvanostatic charge/discharge (GCD) measurements were performed using a LAND CT2001A multichannel battery testing system in the potential window of 0.01–1.5 V (*vs.* Li^+/Li).

SiO_x@NC//$LiFePO_4$ full-cells were also assembled. The SiO_x@NC-based anode was cycled in half-cells for several cycles before full-cell assembly. The cathodes were acquired by mixing $LiFePO_4$, Super P, and poly(vinylidenefluoride) (PVDF) (dissolved in *N*-methyl-2-pyrrolidone) with the mass ratio of 90 : 5 : 5 into a homogeneous slurry, followed by being coated onto an Al foil and drying. The weight ratio of cathode to anode was about 4 : 1. The SiO_x@NC//$LiFePO_4$ full-cells were charged/discharged galvanostatically in the electrochemical window of 2.5–3.8 V at 0.2C (1C = 170 mA g^{-1}). Cyclic voltammetry (CV) was measured using a PGSTAT302N Autolab potentiostat/galvanostat between 0.01 and 2.0 V *vs.* Li^+/Li at a scan rate of 0.1 mV s^{-1}. The electrochemical impedance spectra (EIS) were obtained at a frequency ranging from 10 to 100 kHz with a potential amplitude of 10 mV.

Results and discussion

The SiO_x@NC was synthesized through a scalable solvent-free and flammable gas-free approach (Fig. 1, S1 and S2†). First,

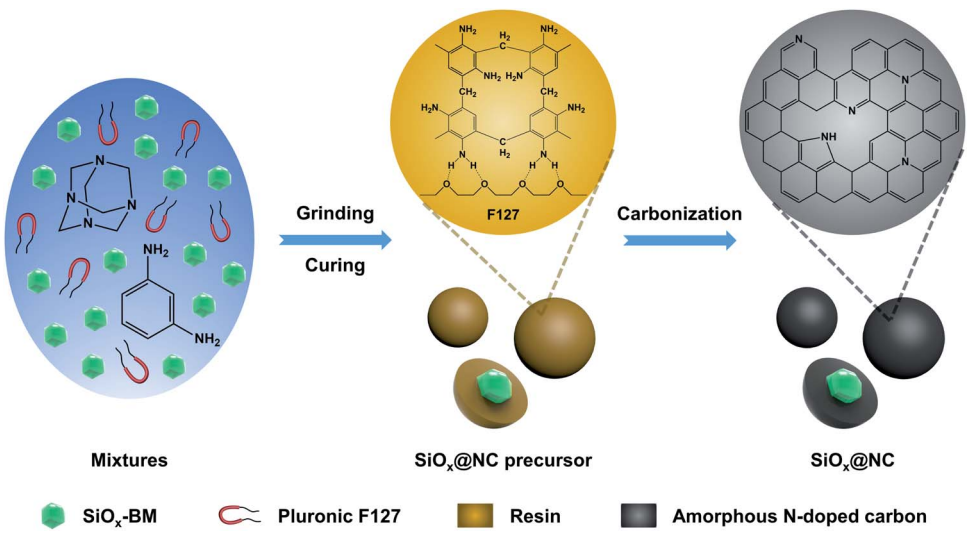

Fig. 1 Schematic illustration for synthesizing SiO_x@NC.

bulk SiO_x was ball milled to obtain SiO_x submicron particles (SiO_x-BM). The SiO_x-BM was then mixed with *m*-phenylenediamine, HMTA, and Pluronic F127 by grinding. With subsequent curing at 160 °C, the HMTA decomposes into ammonia and formaldehyde; the *in situ* generated formaldehyde polymerizes with the *m*-phenylenediamine, forming a *m*-phenylenediamine-formaldehyde resin coating layer on the surface of SiO_x-BM with the assistance of Pluronic F127. After further annealing at 600 °C in Ar, the *m*-phenylenediamine-formaldehyde resin layer is carbonized, and SiO_x@NC with a core@shell structure can be obtained. The whole synthesis process is free of solvent (without waste water generation) and flammable gas, making the scalable production safe and feasible.

Bulk SiO_x has an irregular morphology with relatively sharp edges and it has an average size of ~5 μm (Fig. 2a). The particle size is significantly reduced and the relatively sharp edges disappear after ball milling. The SiO_x-BM shows a particle size of 100–200 nm (Fig. 2b and c). Fig. 2d and e present the HAADF-STEM images of the obtained SiO_x@NC. The SiO_x submicron particles with brighter contrast are fully enveloped in carbon shells with darker contrast, forming a well-defined core@shell structure. The carbon coating shell shows a uniform thickness of ~40 nm and the obtained SiO_x@NC has a size of 200–300 nm, much larger than that of bare SiO_x-BM. EDS spectra were collected at the core region and shell region of an individual SiO_x@NC particle (Fig. 2f). Obviously, the core is composed of SiO_x, while the shell is composed of N-doped carbon. EDS mapping results (Fig. 2g–k) corresponding to Fig. 2d further show that Si and O are mainly distributed at the core area of SiO_x@NC and their signals overlap with each other, whereas C and N are uniformly distributed mainly on the shell, clearly demonstrating the SiO_x@NC core@shell structure. Such a core@shell enveloping structure is highly preferred to tackle the volume variation issue of SiO_x in lithium storage, because the carbon shell has high mechanical stability, high electrical conductivity, and relatively small volume expansion when lithiated.

The carbon content of SiO_x@NC was determined by TGA (Fig. 3a). The bulk SiO_x displays a weight gain of 7.8 wt% from 600 to 1000 °C, and it is caused by the oxidation of SiO_x. As for SiO_x@NC, a sharp weight loss can be observed at ~550 °C, which is caused by the combustion of carbon. The weight loss of SiO_x@NC from 200 to 800 °C reaches 55.4 wt%. No weight gain is observed for SiO_x@NC in the temperature range of 600–1000 °C, indicating the SiO_x is fully oxidized during the combustion of carbon. From TGA, the SiO_x and carbon contents of SiO_x@NC are calculated to be 34.8 wt% and 65.2 wt%, respectively. XRD patterns of SiO_x@NC and bulk SiO_x were

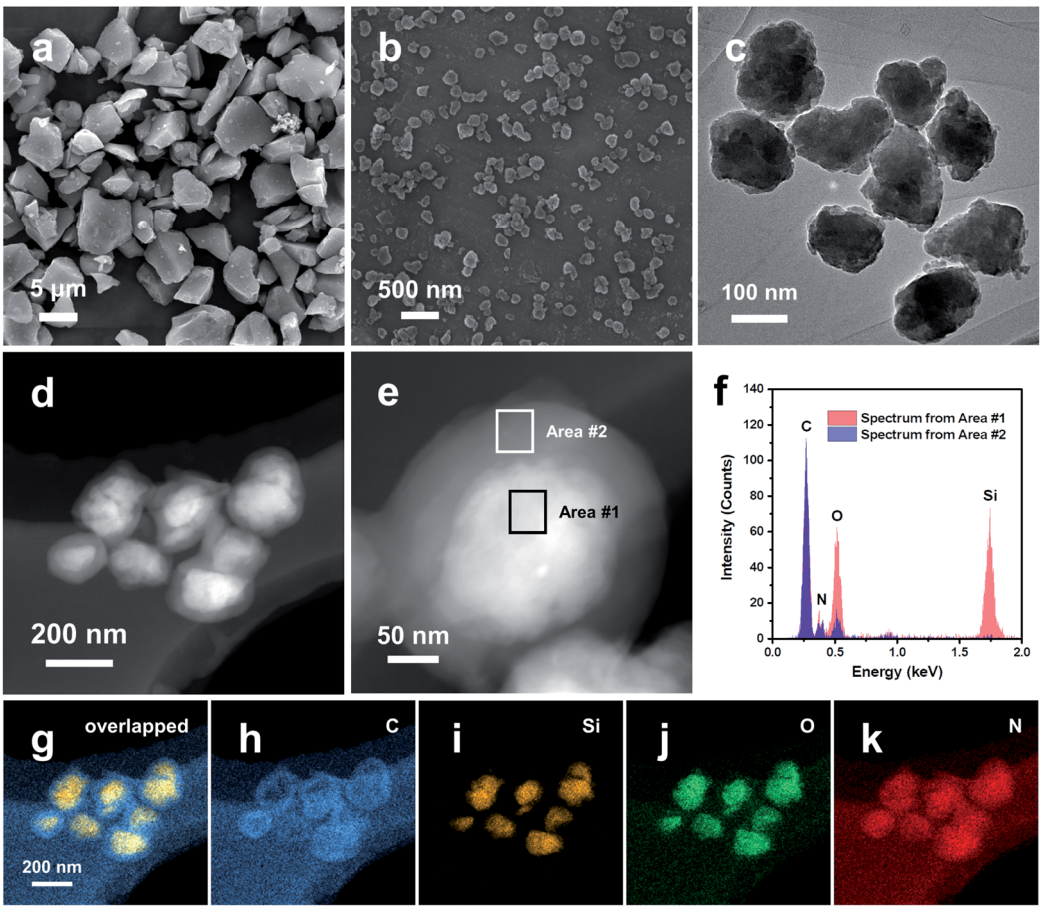

Fig. 2 SEM image of bulk SiO_x (a), SEM (b) and TEM (c) images of SiO_x-BM, HAADF-STEM images (d and e), EDS spectra (f) and EDS mappings (g–k) of SiO_x@NC.

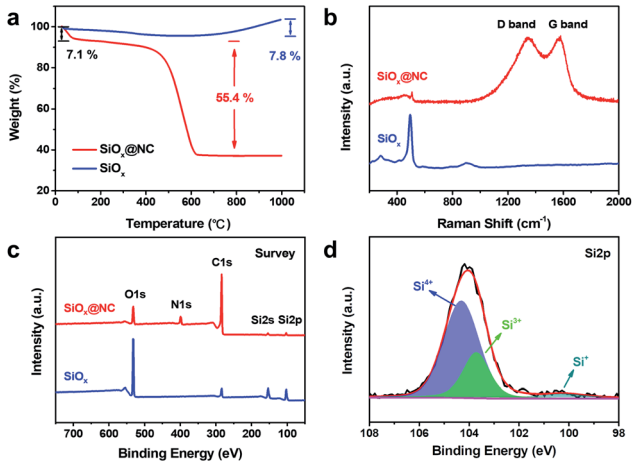

Fig. 3 TGA curves (a) and Raman spectra (b) of SiO_x@NC and bulk SiO_x, XPS survey spectra of SiO_x@NC and bulk SiO_x (c), high-resolution Si 2p XPS spectrum of SiO_x@NC (d).

recorded and presented in Fig. S3.† Both samples display a broad diffraction at $2\theta = 20$–$30°$, which is characteristic for amorphous SiO_x. Although the SiO_x@NC has a relatively high carbon content, no diffractions for graphitic carbon are detected, suggesting the carbon shell is amorphous. Raman spectrum of SiO_x@NC (Fig. 3b) shows a sharp peak at ~500 cm^{-1} and two broad bands at 1338 and 1588 cm^{-1}. The broad peaks are D and G bands of carbon, while the former sharp peak is characteristic for amorphous SiO_x.[46] The intensity of D band is comparable to that of G band, demonstrating the amorphous characteristics of carbon, which agrees well with XRD results. PSD curves of SiO_x-BM and SiO_x@NC are displayed in Fig. S4.† The SiO_x-BM presents a relatively narrow particle size distribution with a peak centred at ~0.28 μm. As for SiO_x@NC, two peaks are observed at 0.4 and 1.3 μm of the PSD curve. The relatively weak peak at 1.3 μm may be caused by the aggregation of particles during the polymerization or carbonization. The BET surface areas of SiO_x@NC and bulk SiO_x were determined by N_2 sorption (Fig. S5†). The surface area of bulk SiO_x is 1.2 m^2 g^{-1}, while that of SiO_x@NC is 24.0 m^2 g^{-1}.

The surface composition of SiO_x@NC and bulk SiO_x were monitored by XPS. The survey spectrum of SiO_x@NC displays a much stronger C 1s peak than SiO_x owing to the high carbon content of the former (Fig. 3c). The Si 2p core level spectrum of bulk SiO_x (Fig. S6†) shows the co-existence of Si^{4+} (104.3 eV), Si^{3+} (103.7 eV), Si^{2+} (102.5 eV), and Si^{+} (100.2 eV).[39] In contrast, only Si^{4+} (104.3 eV), Si^{3+} (103.7 eV), and a small fraction of Si^{+} (100.2 eV) can be detected in SiO_x@NC. The average valence states of Si for bulk SiO_x and SiO_x@NC are 2.77 and 3.51, respectively. The oxidation of Si in SiO_x@NC may occur during the ball milling process. The high-resolution C 1s spectrum of SiO_x@NC (Fig. S7a†) is dominated by sp^2-bonded C (C=C, 284.8 eV).[47] The N 1s spectrum (Fig. S7b†) is dominated by pyrrolic N (N-5, 400.4 eV) and pyridinic N (N-6, 398.4 eV).[48] As for the O 1s spectrum (Fig. S7c†), the peaks at 533.5, 532.8, and 531.4 eV can be attributed to the Si–O–Si, C–O–C, and Si–O–C, respectively.[49]

Fig. 4a displays the initial four CV curves of SiO_x@NC. The two cathodic peaks appeared at 1.2 and 0.48 V in the initial cycle are attributed to the generation of solid electrolyte interphase (SEI) film, which is caused by the decomposition of FEC additive and electrolyte. Both peaks disappear in the following cycles. The cathodic peaks below 0.25 V and the anodic peaks at ~0.33 and 0.51 V correspond to the transformation between Si and Li_xSi. The overlapping CV profiles demonstrate good reversibility of the electrochemical processes. Selected GCD profiles of SiO_x@NC are presented in Fig. 4b. The SiO_x@NC delivers an initial discharge capacity of 1309 mA h g^{-1} and an initial

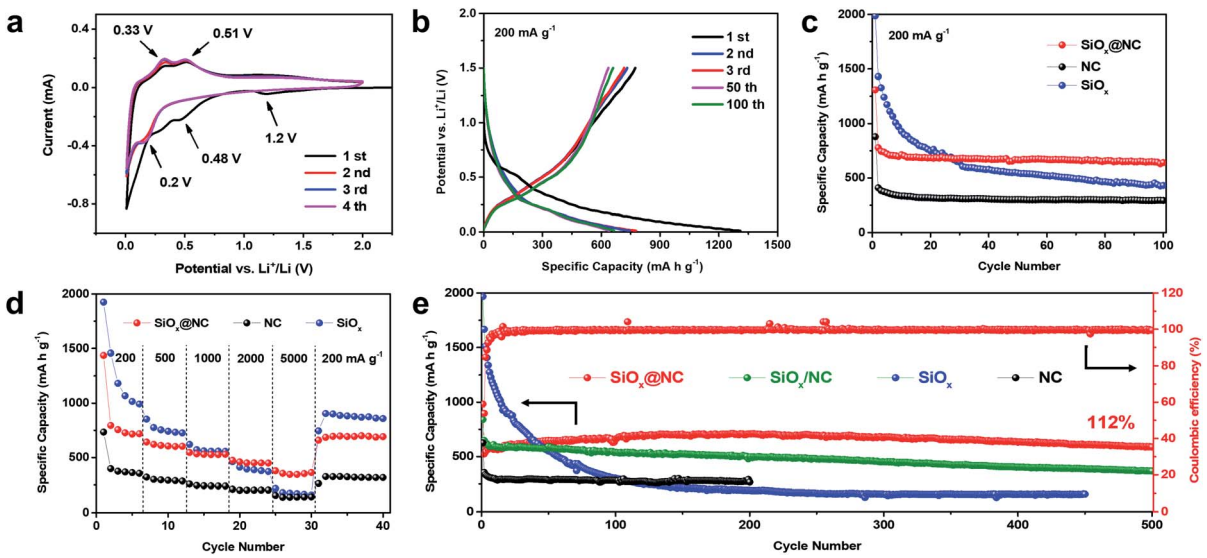

Fig. 4 CV curves of SiO_x@NC in the potential range of 0.01–2.0 V *vs.* Li^+/Li at 0.1 mV s^{-1} (a), selected GCD profiles of SiO_x@NC at 200 mA g^{-1} (b), cycling performances (c) and rate performances (d) of SiO_x@NC, NC and bulk SiO_x, long-term cycling performances of SiO_x@NC, SiO_x/NC physical mixture, bulk SiO_x, and NC at 500 mA g^{-1} (e).

coulombic efficiency (ICE) of 59.1%. Besides the generation of SEI, the low ICE of SiO_x@NC may also be caused by the trap of Li^+ in amorphous carbon. To demonstrate this deduction, pure NC were also prepared by the solvent-free method. The ICE for NC is only 47.2%. For practical applications, the low ICE issue could be solved by pre-lithiation.[50,51] For comparison, selected GCD profiles of NC and bulk SiO_x are provided in Fig. S8 and S9,† respectively. By comparing the discharge profiles (Fig. 4b and S9†), it is not difficult to find that the bulk SiO_x displays a lower discharge plateau than the SiO_x@NC. This is associated with the lower average oxidation state of Si in bulk SiO_x, because the discharge plateau of SiO_x is highly dependent on the valence state of Si.

Fig. 4c compares the cycling performances of SiO_x@NC, bulk SiO_x, and NC at 200 mA g^{-1}. Pure NC delivers a stable capacity of ~300 mA h g^{-1}. Although the bulk SiO_x demonstrates a high reversible capacity of 1431 mA h g^{-1}, the capacity fades quickly with cycling. The SiO_x@NC integrates the advantages of high capacity from SiO_x and excellent cycling stability from NC. It provides a reversible capacity of 774 mA h g^{-1} with very stable cycling performance. The SiO_x@NC also demonstrates excellent rate capability. A high specific capacity of 756 mA h g^{-1} is achieved at 200 mA g^{-1} and a capacity of 345 mA h g^{-1} can be retained at 5000 mA g^{-1} (Fig. 4d and S10†). Fig. 4e shows the cycling performances of SiO_x@NC, SiO_x/NC physical mixture, bulk SiO_x, and NC at 500 mA g^{-1}. The SiO_x@NC presents a much higher capacity than NC, and its high capacity does not compromise the cyclability. It shows negligible capacity decay over 500 cycles, much better than those of bulk SiO_x and SiO_x/NC physical mixture, demonstrating the significant role of carbon coating layer in buffering volume change and improving cyclability. Slight capacity increase with cycle number has been observed for SiO_x@NC in the first 200 cycles. Similar phenomenon has been observed in other high-capacity anode materials as well and it can be ascribed to the reversible growth/dissolution of a polymeric gel-like film.[52,53] The lithium storage performances of SiO_x@NC are compared with previously reported SiO_x in Table S1.† Obviously, the SiO_x@NC demonstrates a comparable lithium storage performance to state-of-the-art SiO_x based anode materials.

To investigate the effect of carbon content on lithium storage, SiO_x@NC with a lower carbon content (higher SiO_x content) has also been prepared. As shown in Fig. S11,† the SiO_x@NC sample with a lower carbon content delivers a higher specific capacity in lithium storage; however, it sacrifices the cycling stability a little bit.

The Nyquist plots of SiO_x@NC and bulk SiO_x before and after cycling are provided in Fig. S12 and S13.† The high-frequency semi-circle corresponds to the charge-transfer resistance (R_{ct}) at the electrode and electrolyte interface.[54] The low-frequency straight line stands for Warburg impedance (W), and its slope reflects the Li^+ diffusivity. Before cycling, the SiO_x@NC shows an obvious smaller R_{ct} (39.27 Ω) and W (0.32 Ω) against bulk SiO_x (R_{ct}: 100.8 Ω, W: 0.41 Ω), suggesting its higher electronic conductivity and faster Li^+ diffusion kinetic. After 100 cycles (Fig. S13†), the R_{ct} of bulk SiO_x increases rapidly from 100.8 Ω to 292.5 Ω. In contrast, the R_{ct} of SiO_x@NC only increases from 39.27 Ω to 57.66 Ω, demonstrating the positive impact of NC on enhancing the conductivity and constraining the volume change of SiO_x.

For anode materials, the high capacity is always accompanied by undesirable large volume variation. As a result, most high-capacity anode materials suffer from unsatisfactory structural stability and cyclability. To investigate the structure integrity of the SiO_x@NC, SEM images before and after 100 cycles are collected (Fig. S14†). Furthermore, HAADF-STEM images and EDS mappings of bulk SiO_x and SiO_x@NC after 100 cycles are also presented in Fig. S15.† Serious pulverization and cracking are observed for bulk SiO_x after cycling (Fig. S14b and S15a†), which might be the origin of rapid capacity decay observed in Fig. 4c. In contrast, the SiO_x@NC shows excellent structural stability; its size and morphology is well maintained after cycling (Fig. S14d and S15e†). The *ex situ* SEM and *ex situ* TEM results clearly demonstrate the significant role of carbon encapsulation in buffering volume change and improving cyclability. Cross-sectional SEM images of the electrodes before cycling and after 100 cycles are also provided. The thickness of bulk SiO_x-based electrode increases from 7.0 to 10.9 μm, corresponding to a 55.7% thickness expansion (Fig. S16a and b†). In addition, serious peeling off of the active material from the

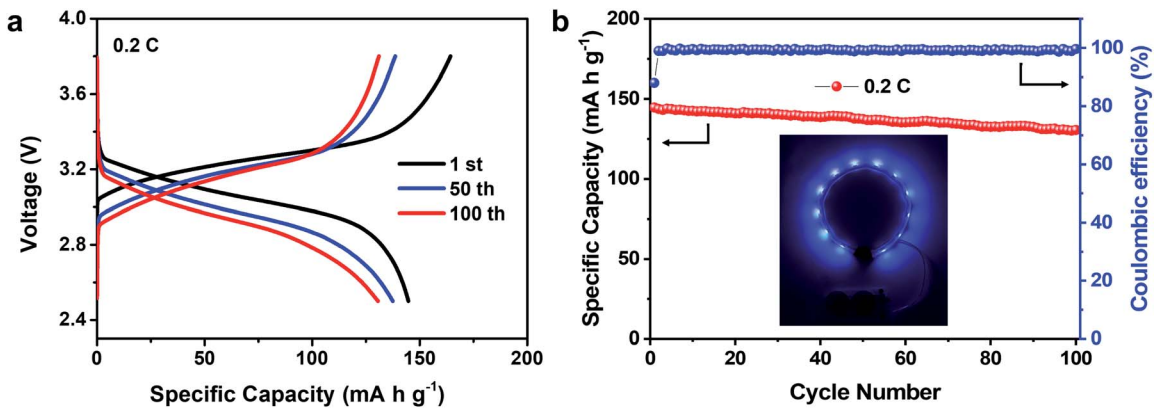

Fig. 5 Selected GCD profiles (a) and cycling performance (b) of a SiO_x@NC//$LiFePO_4$ full-cell at 0.2C, the LED belts are powered by two SiO_x@NC//$LiFePO_4$ coin cells.

Cu collector and electrode cracking can be observed (Fig. S16b†). Under similar conditions, the SiO_x@NC-based electrode shows only 14.1% thickness expansion after 100 cycles (from 9.9 to 11.3 μm, Fig. S16c and d†). The above results demonstrate that enveloping SiO_x in mechanically robust carbon can buffer its volume variation during cycling and thus improves the structural stability and electrode integrity.

To further verify the potential of SiO_x@NC in LIBs, SiO_x@NC//$LiFePO_4$ full-cells were assembled, and the electrochemical performances of $LiFePO_4$ are displayed in Fig. S17.† Before full-cell assembly, the SiO_x@NC was cycled in half-cells for several cycles to avoid the irreversible Li^+ consumption in the initial cycle. Fig. 5a presents the charge–discharge profiles of the full-cell; a relatively flat discharge plateaus can be observed at 2.9–3.3 V. The cycling stability of full cell is tested at 0.2C for 100 cycles between 2.5 and 3.8 V. Based on the mass of $LiFePO_4$, the full-cell demonstrates a capacity of 145 mA h g^{-1} at 0.2C and 90.2% of the capacity can be maintained after 100 cycles.

Conclusions

In summary, an eco-friendly and scalable solvent-free, flammable gas-free approach has been developed to envelop SiO_x submicron particles in N-doped carbon. The enveloping structure improves the electrical conductivity and buffers the large volume expansion of SiO_x, resulting in significantly enhanced structural stability and electrode integrity. As a result, the obtained SiO_x@NC manifests high specific capacity as well as excellent durability. A stable high capacity of ~709 mA h g^{-1} can be achieved at 200 mA g^{-1}; negligible capacity decay is demonstrated for 500 cycles at 500 mA g^{-1}. The eco-friendly and scalable synthesis as well as the impressive lithium storage performances make the SiO_x@NC a competitive LIB anode material. It is anticipated that the solvent-free approach developed here can also be generally applied to other high-capacity anode materials, such as Si, Sn, and Sb.

Conflicts of interest

There are no conflicts to declare.

Acknowledgements

This work was supported by the National Key Research and Development Program of China (2018YFB0104200), the National Natural Science Foundation of China (21673171) and the Foshan Xianhu Laboratory of the Advanced Energy Science and Technology Guangdong Laboratory (XHT2020-003).

Notes and references

1 J. B. Goodenough and Y. Kim, *Chem. Mater.*, 2009, **22**, 587–603.
2 Y. Sun, N. Liu and Y. Cui, *Nat. Energy*, 2016, **1**, 16071.
3 B. Dunn, H. Kamath and J. M. Tarascon, *Science*, 2011, **334**, 928–935.
4 J. B. Goodenough and K. S. Park, *J. Am. Chem. Soc.*, 2013, **135**, 1167–1176.
5 Z. Yang, J. Zhang, M. C. Kintner-Meyer, X. Lu, D. Choi, J. P. Lemmon and J. Liu, *Chem. Rev.*, 2011, **111**, 3577–3613.
6 J. Lee, J. Moon, S. A. Han, J. Kim, V. Malgras, Y. U. Heo, H. Kim, S. M. Lee, H. Liu, S. Dou, Y. Yamauchi, M. S. Park and J. H. Kim, *ACS Nano*, 2019, **13**, 9607–9619.
7 J. Wu, Y. Cao, H. Zhao, J. Mao and Z. Guo, *Carbon Energy*, 2019, **1**, 57–76.
8 M. Li, Y. Zeng, Y. Ren, C. Zeng, J. Gu, X. Feng and H. He, *J. Power Sources*, 2015, **288**, 53–61.
9 M. Han and J. Yu, *J. Power Sources*, 2019, **414**, 435–443.
10 Z. Yan, H. Jin and J. Guo, *Carbon Energy*, 2019, **1**, 246–252.
11 M. Armand and J. Tarascon, *Nature*, 2008, **451**, 652–657.
12 Y. Zhang, F. Du, X. Yan, Y. Jin, K. Zhu, X. Wang, H. Li, G. Chen, C. Wang and Y. Wei, *ACS Appl. Mater. Interfaces*, 2014, **6**, 4458–4465.
13 K. S. Novoselov, A. K. Geim, S. V. Morozov, D. Jiang, Y. Zhang, S. V. Dubonos, I. V. Grigorieva and A. A. Firsov, *Science*, 2004, **306**, 666–669.
14 L. Zhang, J. Deng, L. Liu, W. Si, S. Oswald, L. Xi, M. Kundu, G. Ma, T. Gemming, S. Baunack, F. Ding, C. Yan and O. G. Schmidt, *Adv. Mater.*, 2014, **26**, 4527–4532.
15 H. Zhang, K. Liu, Y. Liu, Z. Lang, W. He, L. Ma, J. Man, G. Jia, J. Cui and J. Sun, *J. Power Sources*, 2020, **447**, 227400.
16 R. Fu, Y. Li, Y. Wu, C. Shen, C. Fan and Z. Liu, *J. Power Sources*, 2019, **432**, 65–72.
17 Z. Liu, Y. Zhao, R. He, W. Luo, J. Meng, Q. Yu, D. Zhao, L. Zhou and L. Mai, *Energy Storage Materials*, 2019, **19**, 299–305.
18 G. Zhu, F. Zhang, X. Li, W. Luo, L. Li, H. Zhang, L. Wang, Y. Wang, W. Jiang, H. K. Liu, S. Dou and J. Yang, *Angew. Chem., Int. Ed.*, 2019, **58**, 6669–6673.
19 W. He, Y. Liang, H. Tian, S. Zhang, Z. Meng and W. Han, *Energy Storage Materials*, 2017, **8**, 119–126.
20 H. Zhang, R. Hu, Y. Liu, X. Cheng, J. Liu, Z. Lu, M. Zeng, L. Yang, J. Liu and M. Zhu, *Energy Storage Materials*, 2018, **13**, 257–266.
21 J. I. Lee, K. T. Lee, J. Cho, J. Kim, N. S. Choi and S. Park, *Angew. Chem., Int. Ed.*, 2012, **51**, 2767–2771.
22 J. I. Lee and S. Park, *Nano Energy*, 2013, **2**, 146–152.
23 J. Zhang, C. Zhang, Z. Liu, J. Zheng, Y. Zuo, C. Xue, C. Li and B. Cheng, *J. Power Sources*, 2017, **339**, 86–92.
24 Z. Liu, D. Guan, Q. Yu, L. Xu, Z. Zhuang, T. Zhu, D. Zhao, L. Zhou and L. Mai, *Energy Storage Materials*, 2018, **13**, 112–118.
25 Q. Xu, J. Sun, Y. Yin and Y. Guo, *Adv. Funct. Mater.*, 2018, **28**, 1705235.
26 Q. Yu, P. Ge, Z. Liu, M. Xu, W. Yang, L. Zhou, D. Zhao and L. Mai, *J. Mater. Chem. A*, 2018, **6**, 14903–14909.
27 Z. Liu, Q. Yu, Y. Zhao, R. He, M. Xu, S. Feng, S. Li, L. Zhou and L. Mai, *Chem. Soc. Rev.*, 2019, **48**, 285–309.
28 Z. Li, Q. He, L. He, P. Hu, W. Li, H. Yan, X. Peng, C. Huang and L. Mai, *J. Mater. Chem. A*, 2017, **5**, 4183–4189.
29 W. An, J. Fu, J. Su, L. Wang, X. Peng, K. Wu, Q. Chen, Y. Bi, B. Gao and X. Zhang, *J. Power Sources*, 2017, **345**, 227–236.

30 T. Chen, J. Wu, Q. Zhang and X. Su, *J. Power Sources*, 2017, **363**, 126–144.
31 C. Tang, Y. Liu, C. Xu, J. Zhu, X. Wei, L. Zhou, L. He, W. Yang and L. Mai, *Adv. Funct. Mater.*, 2018, **28**, 1704561.
32 X. Su, Q. Wu, J. Li, X. Xiao, A. Lott, W. Lu, B. W. Sheldon and J. Wu, *Adv. Energy Mater.*, 2014, **4**, 1300882.
33 P. Lv, H. Zhao, C. Gao, Z. Du, J. Wang and X. Liu, *J. Power Sources*, 2015, **274**, 542–550.
34 C. Gao, H. Zhao, P. Lv, C. Wang, J. Wang, T. Zhang and Q. Xia, *J. Electrochem. Soc.*, 2014, **161**, A2216–A2221.
35 J. Wang, H. Zhao, J. He, C. Wang and J. Wang, *J. Power Sources*, 2011, **196**, 4811–4815.
36 E. Park, H. Yoo, J. Lee, M. S. Park, Y. J. Kim and H. Kim, *ACS Nano*, 2015, **9**, 7690–7696.
37 J. Cui, Y. Cui, S. Li, H. Sun, Z. Wen and J. Sun, *ACS Appl. Mater. Interfaces*, 2016, **8**, 30239–30247.
38 Y. Ju, J. A. Tang, K. Zhu, Y. Meng, C. Wang, G. Chen, Y. Wei and Y. Gao, *Electrochim. Acta*, 2016, **191**, 411–416.
39 Y. Ren and M. Li, *J. Power Sources*, 2016, **306**, 459–466.
40 C. Guo, D. Wang, T. Liu, J. Zhu and X. Lang, *J. Mater. Chem. A*, 2014, **2**, 3521–3527.
41 I. Choi, M. J. Lee, S. M. Oh and J. J. Kim, *Electrochim. Acta*, 2012, **85**, 369–376.
42 K. W. Kim, H. Park, J. G. Lee, J. Kim, Y. U. Kim, J. H. Ryu, J. J. Kim and S. M. Oh, *Electrochim. Acta*, 2013, **103**, 226–230.
43 L. Shi, C. Pang, S. Chen, M. Wang, K. Wang, Z. Tan, P. Gao, J. Ren, Y. Huang, H. Peng and Z. Liu, *Nano Lett.*, 2017, **17**, 3681–3687.
44 Q. Xu, J. Sun, Z. Yu, Y. Yin, S. Xin, S. Yu and Y. Guo, *Adv. Mater.*, 2018, **30**, 1707430.
45 G. Li, J. Li, F. Yue, Q. Xu, T. Zuo, Y. Yin and Y. Guo, *Nano Energy*, 2019, **60**, 485–492.
46 X. Liu, M. Zheng, K. Xie and J. Liu, *Electrochim. Acta*, 2012, **59**, 304–309.
47 J. Wang, H. Liu, J. Diao, X. Gu, H. Wang, J. Rong, B. Zong and D. Su, *J. Mater. Chem. A*, 2015, **3**, 2305–2313.
48 N. P. Wickramaratne, J. Xu, M. Wang, L. Zhu, L. Dai and M. Jaroniec, *Chem. Mater.*, 2014, **26**, 2820–2828.
49 Q. Xia, B. Wang, Y. Wu, H. Luo, S. Zhao and T. Ree, *J. Power Sources*, 2008, **180**, 602–606.
50 Q. Meng, G. Li, J. Yue, Q. Xu, Y. Yin and Y. Guo, *ACS Appl. Mater. Interfaces*, 2019, **11**, 32062–32068.
51 H. J. Kim, S. Choi, S. J. Lee, M. W. Seo, J. G. Lee, E. Deniz, Y. J. Lee, E. K. Kim and J. W. Choi, *Nano Lett.*, 2015, **16**, 282–288.
52 S. Laruelle, S. Grugeon, P. Poizot, M. Dolle, L. Dupont and J. M. Tarascon, *J. Electrochem. Soc.*, 2002, **149**, A627–A634.
53 S. Grugeon, S. Laruelle, L. Dupont and J. M. Tarascon, *Solid State Sci.*, 2003, **5**, 895–904.
54 X. Cao, X. Chuan, S. Li, D. Huang and G. Cao, *Part. Part. Syst. Charact.*, 2016, **33**, 110–117.